Responses to Flow Interventions for Shock Train Modulation in a Supersonic Isolator

Fuhao Chen*, Zhaoyang Tian*, Rui Ran* and Lei Shi*
Corresponding author: shilei@nwpu.edu.cn
* National Key Laboratory of Solid Rocket Propulsion, Northwestern Polytechnical University, Xi'an, Shaanxi 710072, People's Republic of China.

Abstract: In practical ramjet engines, combustion instabilities induce significant pressure oscillations, which affect the shock train structure in the isolator and introduce considerable operational risks. This study investigates the modulation of the shock train in an isolator using suction and injection. The results demonstrate that both flow intervention methods are effective but operate through distinct mechanisms. Suction creates a low-pressure zone, removes the near-wall boundary layer, and suppresses flow separation, thereby stabilizing the shock train downstream (7.62%L) and enhancing its stability. In contrast, microjet injection establishes a favorable pressure gradient zone, which shifts the shock train downstream with a smaller displacement (2.70%L). The larger separation bubble on one side within the shock train demonstrates significantly greater streamwise development, whereas the smaller one on the opposite wall expands predominantly in the spanwise direction. While suction simplifies design and improves stability, it incurs flow loss. Conversely, injection preserves the captured airflow but brings flow unsteadiness. Suction and injection both can reduce flow distortion and improve flow quality at the exit when the shock train is effectively controlled. Suction effectively dampens self-excited oscillations by removing part of the leading-edge separation bubble, whereas injection introduces additional unsteadiness. They both concentrate the oscillation intensity in the shock train leading edge. The oscillation frequency of the separation bubble (30-40 Hz) is markedly lower than both the primary (360-393 Hz) and secondary (131-139 Hz) characteristic frequencies of the leading-edge shock wave. Resolving this multi-scale characteristic is fundamental to constructing a comprehensive physical model of the shock train phenomenon.

Keywords: Shock train, Suction, Microjet injection, Self-excited oscillation.

Nomenclature	
L	Length of the isolator, mm
x	Distance from entrance of isolator test section, mm
p_0	Incoming flow static pressure, Pa
p_w	Wall static pressure, Pa
p_i	Injection total pressure, Pa
p_e	Exit flow total pressure, Pa
$\bar{D}$	Total pressure distortion index
Abbreviation	
SWBLI	Shock wave/boundary layer interaction
CVP	Counter-rotating vortex pair
PR	Dimensionless static pressure ratio
GCI	Grid convergence index
MPR	Dimensionless microjet pressure ratio
PSD	Power spectral density

1. Introduction

The isolator, a critical component in ramjet engines, facilitates flow deceleration and pressurization through the formation of an internal shock train. Its operational efficiency has a direct impact on combustion and overall engine performance. The shock train represents a classic case of shock wave/boundary layer interaction (SWBLI)[1], characterized by highly complex, three-dimensional flow structures including compression and expansion waves, boundary layers, and separation bubbles. Both upstream inflow conditions and downstream pressure states govern the characteristics and configuration of the shock train. Furthermore, the inherent instability of SWBLI induces intense oscillations throughout the shock system. Therefore, maintaining a stable and controllable shock train is crucial for ensuring engine safety and operational effectiveness. The stabilization of a shock train presents greater challenges compared to isolated SWBLI cases due to its increased complexity. In response, numerous flow control strategies have been explored to improve and stabilize these flow fields. These approaches are broadly categorized into passive methods—such as suction[2, 3], cavities[4, 5, 6], and vortex generators[7, 8, 9]—and active methods, including microjets[10, 11, 12], magnetic fluids[13], plasma actuation[14, 15, 16], energy deposition[17], and deformable structure[18, 19].

Extensive research has been devoted to understanding the characteristics and structure of the shock train, employing theoretical analysis, numerical simulations, and experimental methods. These studies have established that key attributes such as the formation, location, and oscillation behavior of the shock train are influenced by a range of factors, including the incoming flow conditions[20, 21, 22], background waves[23], downstream backpressure[24, 25], three-dimensional flow effects[26], and the specific geometry of the channel[27]. A substantial body of research on shock trains underscores the necessity of flow intervention for modern aircraft, which must operate across wide speed ranges and vast airspace with high performance. Flow control techniques[28] are pivotal in this regard, as they augment the dynamic characteristics of inherently unstable flow regions and expand the stable operational envelope, thereby mitigating or even eliminating zones of instability. In practice, passive control achieves this energy redistribution through tailored geometric designs, while active control introduces auxiliary energy to directly influence and stabilize the target flow areas.

Tan *et al.*[29] emphasized the non-negligible influence of background waves on shock train characteristics, even within direct-connect test facilities, highlighting that disturbing waves inevitably altered its structure and motion. Huang *et al.*[30] further probed the shock train's dynamic behavior under such conditions. Their investigation discerned an "energy-level-transition-like" process during its upstream movement and identified three distinct motion modes as the shock train traversed a reflection point: continuous forward motion, low-frequency oscillatory forward motion, and rapid forward motion. Wang *et al.*[31, 32, 33] investigated the impacts of various factors—including incoming *Mach* number, background waves, variational backpressure, three-dimensional geometry, and incident shocks—on both the steady-state structure and dynamic characteristics of the shock train. Their findings indicated that the overall movement trend of the shock train was governed by the incoming *Mach* number and the mean backpressure, while the oscillation feedback mechanism was attributed to acoustic wave propagation and the duct volume effect. Wang *et al.*[34] contrasted the effects of different incident shock patterns: unilateral incident shocks induced a more intense oscillation with a lower dominant frequency, whereas symmetric bilateral shocks enhanced structural symmetry while concurrently suppressing oscillation strength. To elucidate the fundamental mechanism behind shock train instability, Li *et al.*[35, 36] conducted a detailed investigation into its dynamics. A key finding was the superior capability of a wall-pressure-based model in tracking shock train location, compared to conventional models dependent on exit backpressure. This work further explored the hysteresis behavior of the separation shock by integrating experimental and theoretical study. Hunt and Gamba[37] identified that the inherent unsteadiness of the shock train under constant conditions was driven by a complex, frequency-dependent dynamical system. Key perturbations causing shock train fluctuations included: upstream propagating acoustic waves from separation bubbles; vortices shed from these bubbles and convect downstream; upstream propagating acoustic waves generated in the diffuser.

In light of these complex dynamics, several flow intervention methods have been explored to manage shock-induced separation and unsteadiness. The work of Weiss and Olivier[38] demonstrated that a normal suction slot can stabilize a shock train in supersonic flow. When the suction pressure was low enough, the primary shock foot was stabilized, allowing the shock train to transition into a single normal shock to match the higher backpressure. A flow model was derived to predict this transition, calculate the required suction mass flow, and determine the resulting total pressure losses. Sethuraman *et al.*[39] found that boundary layer suction effectively controlled shock train oscillation by restricting its bifurcation. A higher suction ratio transformed it into a single shock and raised the dominant frequency, while a lower ratio introduced new opposing pressure disturbances and lateral oscillations that altered the system's dynamics. He *et al.*[40] conducted the numerical simulation in a constant-area isolator with asymmetric configuration and highlighted the critical role of 3D geometry and viscous effects on shock train dynamics. They found that flow separation was predominant at the upper wall corner due to asymmetric boundary layer development. Spanwise suction on the side wall was confirmed to significantly shorten the shock train by removing low-momentum corner fluid, thereby exerting control over the SWBLI.

Xu *et al.*[41] reviewed recent studies on microjet flow control for SWBLI. Although microjets were geometrically small, their effectiveness in modulating flow fields had been validated through both experimental studies and numerical simulations. The underlying mechanism of microjet injection control lied in the formation of an unsteady counter-rotating vortex pair (CVP) as the injected flow interacted with the mainstream[42]. The CVP moved along the flow direction and facilitated momentum exchange between the high-momentum fluid and the boundary layer. This process was conducive to the boundary layer resisting the adverse pressure gradient and reduced the extent of flow separation. Verma and Manisankar[43] experimentally demonstrated that a specific array arrangement of steady microjets effectively controlled the flow separation induced by a compression ramp by simultaneously reducing both the extent of separation and the shock unsteadiness.

In summary, while the inherent characteristics of shock trains have been extensively documented, their pronounced unsteady behavior continues to pose considerable challenges to operational stability. Previous research has predominantly focused on mechanism investigations within simplified configurations. There remains a notable scarcity of studies on flow control, particularly regarding its efficacy in influencing the instability characteristics of shock trains—a knowledge gap critical for ensuring stable engine operation. It is thus imperative to verify the control capabilities of suction and injection techniques within complex flow environments. To this end, the present paper combines direct-connect experiments and numerical simulations to examine shock train characteristics and assesses the control effectiveness of suction and injection in a highly confined rectangular duct.

2. Experimental setup

2.1 Experimental apparatus and conditions

All experiments are conducted in a direct-connect supersonic test facility at Northwestern Polytechnical University. The system is supplied with high-pressure air from a storage tank, delivered through a series of pipelines and control valves into the test section. A throttle valve maintains a constant mass flow rate of 0.86 kg/s under an upstream static pressure of 6 MPa. A Laval nozzle is designed to generate the exit Mach number of 2.5. The isolator test section has a rectangular cross-section of 30 mm wide × 30 mm high × 357 mm long (L). Two square flow control ports (30 mm × 30 mm) are machined on both the top and bottom walls, with their upstream edges located 94 mm from the isolator entrance.

A total of 26 pressure transducers is arranged along the top wall centerline to record static pressure distributions. The first transducer (T1) is positioned 15 mm downstream of the isolator entrance, and the last (T26) is placed 15 mm upstream of the exit, with an equal spacing of 10 mm between most sensors. However, the distance between T6 and T7 is increased to 87 mm to accommodate the structural cover near the control port.

Parameter	Value
Mach Number	2.5
static pressure (Pa)	80260.73
flow rate (kg/s)	0.86

Table 1: The flow parameters at the isolator test section inlet.

Two rectangular optical windows (28 mm × 308 mm) are placed on both sidewalls to provide optical access for flow visualization. The window extends from 20 mm to 328 mm downstream of the entrance so that the primary region of interest—near the control port and its downstream development—is fully observable. Flow characteristics in both upstream and downstream regions are captured using high-frequency pressure transducers and a high-speed camera, enabling both qualitative and quantitative analysis of the shock train and flow control methods. A motor-driven plug provides controlled backpressure at a fixed displacement speed. The detailed layout and dimensions are illustrated in figure 1.

To investigate the effectiveness of different intervention methods on the isolator, three types of covers are designed. In this study, two uncontrol covers, two suction covers and an injection connector are used. The characteristics and mechanism of suction and injection can be elucidated through comparative analysis.

The uncontrol cover consists of a lower plug with a 30 mm × 30 mm cross section, with its bottom surface flush with the flow channel. The top section comprises sealing and connection mechanisms. The suction cover employs a two-dimensional vertical slot with a width of 5 mm. An expansion angle is incorporated near the outlet to facilitate smooth airflow overflow, as illustrated in figure 2. The suction slot outlet is directly exposed to the atmosphere. Driven by the pressure difference between the static pressure within the isolator and the atmospheric pressure, a portion of the flow is discharged along the slot.

After optimization and consideration of practical machining capabilities, the two-dimensional microjet scheme with a 5° inclination angle is implemented. The injection slit is 3 mm wide along the flow direction. The working material is accelerated in the channel under the drive of a high-pressure air source and enters the isolator at a slight angle to the mainstream along the slit. This injection angle is selected to keep the injected flow attached to the wall, thereby influencing the near-wall flow without causing blockage, as shown in figure 2. Considering structural integrity requirements, reinforcements are added around the injection slit while minimizing impact on the designed flow path. Specific measures include installing four 1-mm-thick stiffeners in the slit and applying edge blending at the sharp edge of the slit where stress is prone to concentration. The injection connector is connected to high-pressure nitrogen as the working material from a gas bottle. The actual installation during experiments is depicted in figure 3.

Three experimental cases are designed in this study: a contrast case with two uncontrol covers and two experimental cases with two suction covers and one injection connector, respectively. The actual flow conditions at the inlet of the isolator test section in these experiments are presented in table 1. The plug is manipulated remotely to move upstream from the isolator exit and throttles the internal flow, thereby simulating the backpressure. The control effect of suction and injection is specifically investigated based on experimental and numerical results.

2.2 Wall static pressure measurements

In supersonic flow experiments, obtaining quantitative flow field characteristics relies critically on precise pressure measurements. The test section is therefore instrumented with an array of high-precision pressure transducers, each with an operational range of -0.1 to 1 MPa and a comprehensive accuracy of ±0.25% of the full scale. All transducers are pre-calibrated by the manufacturer to ensure data reliability. Pressure signals are acquired using an IOLITE R12 data acquisition and real-time control system, with a sampling frequency of 20 kHz. This configuration provides sufficient temporal resolution to capture subtle fluctuations in wall pressure.

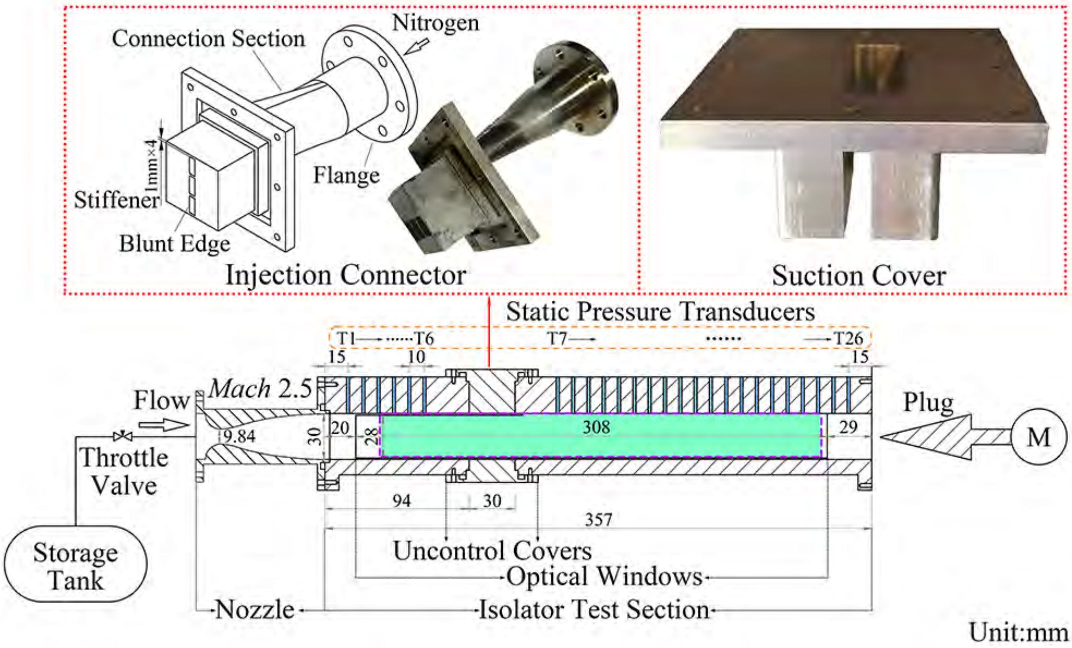

Figure 1: The schematic diagram of the isolator model installed at the direct-connect test facility.

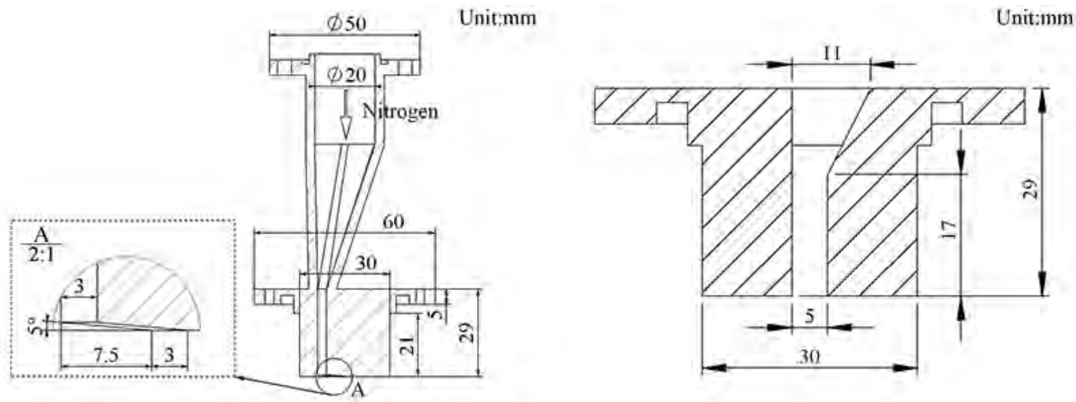

Figure 2: The geometric schematic diagram of the injection connector and the suction cover.

2.3 High-speed schlieren visualization

The supersonic flow field is characterized by its sensitivity to minor disturbances, which generate waves and induce spatial variations in flow parameters. When a light ray propagates through such a heterogeneous, density-gradient field, refraction occurs due to the direct relationship between the refractive index and the fluid density. The schlieren technique exploits this principle to visualize flow inhomogeneities by converting density gradients into measurable variations in light intensity. A schematic of the reflective schlieren measurement light path is presented in figure 4, illustrating an optical setup commonly employed for investigating shock wave systems.

The core components of the implemented Z-type reflective schlieren system comprise a light source, two concave mirrors, a mechanical slit, a knife edge, and a high-speed camera. The optical path originates from a point source, where a narrow beam is spatially filtered through a slit to ensure phase coherence. This beam is then collimated by the first concave mirror and directed through the test section. Upon exiting, the light—now modulated by the density gradients in the flow—is focused by the second concave mirror. A horizontal knife edge is precisely positioned at the focal point, where the light converges to its smallest and brightest spot, to selectively block a portion of the beam. This configuration selectively

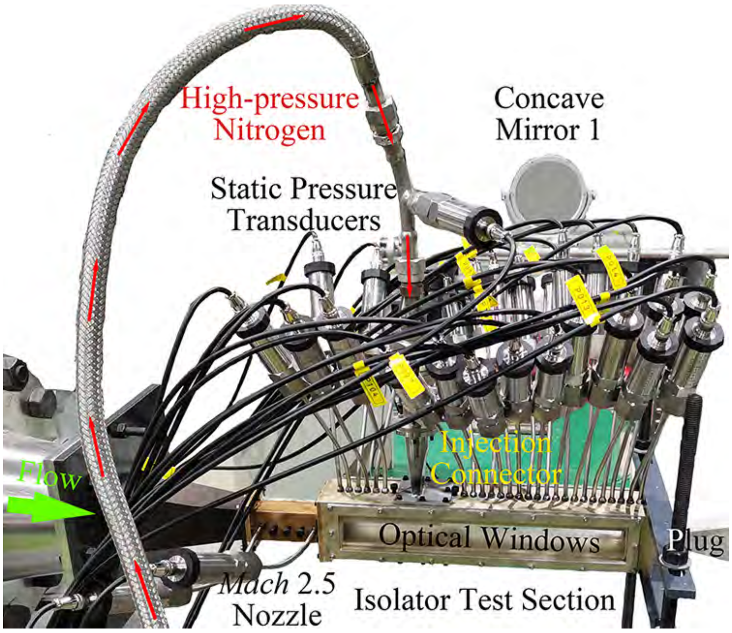

Figure 3: The installation photograph of the injection system.

highlights the vertical components of the density gradient, rendering them visible as variations in light intensity. The resulting schlieren images are captured by a Phantom M340 high-speed camera at a frame rate of 1000 fps with an exposure time of 200 μs, a setup capable of effectively resolving the transient characteristics of the shock train.

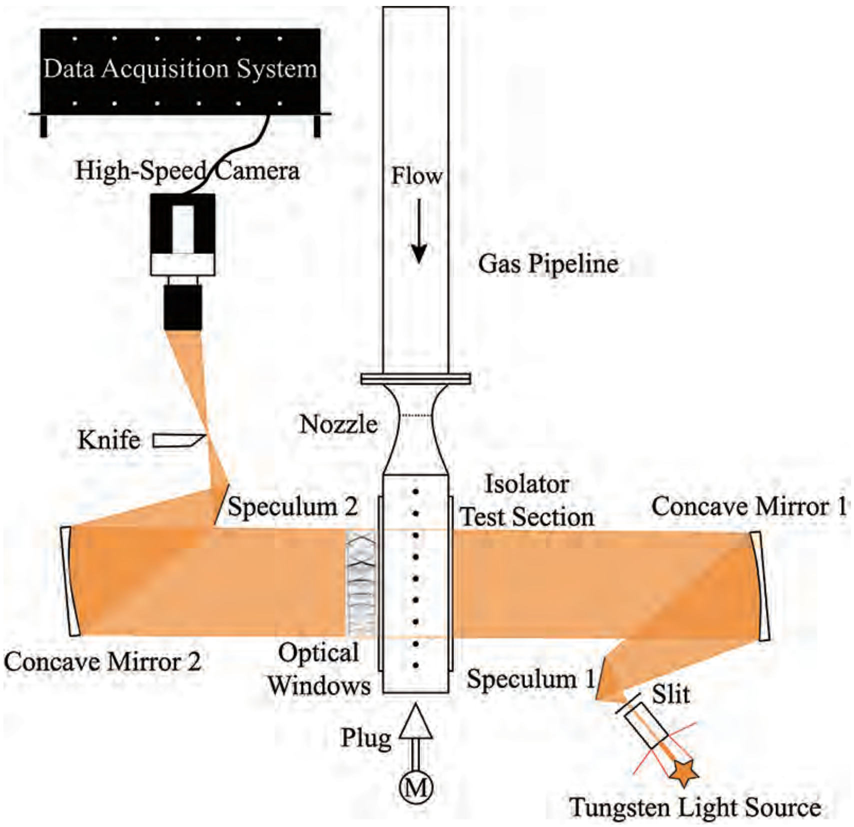

Figure 4: The schematic diagram and the experimental picture of the reflective schlieren system.

3. Numerical simulation setup

3.1 Introduction of the numerical simulation

Based on previous studies, a series of steady three-dimensional Reynolds-Averaged Navier Stokes simulations are performed under different conditions. In this study, all numerical calculations are conducted using the commercial software Fluent for the flow field in the isolator. The flow solver adopted is a three-dimensional, steady, density-based, implicit, structured, Navier–Stokes code using the finite volume approach. The steady compressible Navier-Stokes equations can be described as below.

The mass equation is

$$\nabla \cdot (\rho \vec{v}) = 0 \tag{1}$$

The momentum equation is

$$\nabla \cdot (\rho \vec{v}\vec{v}) = -\nabla p + \nabla \cdot (\tau) \tag{2}$$

The energy equation is

$$\nabla \cdot (\vec{v}(\rho E + p)) = \nabla \cdot (k\nabla T + (\tau \cdot \vec{v})) \tag{3}$$

Here ρ, p, E, T, k, τ and $\vec{v}$ represent the density, pressure, energy, temperature, thermal conductivity, shear stress and velocity, respectively.

Considering the high Reynolds number in supersonic direct-connect test facility and the interference from ramp shocks and cowl shocks in actual operating conditions, the boundary layers in the isolator show fully developed turbulent behavior. Therefore, the calculation employs the two equations $k-\omega$ shear stress transport turbulence model, which integrates multiple approaches: Wilcox's original $k-\omega$ model in the near-wall boundary layer region; the standard $k-\varepsilon$ model outside the boundary layer part to avoid the original $k-\omega$ model's significant sensitivity to the main flow. The model is featured with an advanced treatment that automatically switches between the low and high Reynolds number region. The SST $k-\omega$ model has been demonstrated to exhibit excellent prediction performance in the flow separation region due to adverse pressure gradient and complex supersonic flow field which is caused by the impingement of the shock waves. Its general form in the Cartesian tensor form is

$$\frac{\partial}{\partial t}(\rho k) + \frac{\partial}{\partial x_i}(\rho k u_i) = \frac{\partial}{\partial x_j}\left(\Gamma_k \frac{\partial k}{\partial x_j}\right) + \widetilde{G}_k - Y_k + S_k \tag{4}$$

$$\frac{\partial}{\partial t}(\rho \omega) + \frac{\partial}{\partial x_i}(\rho \omega u_i) = \frac{\partial}{\partial x_j}\left(\Gamma_\omega \frac{\partial \omega}{\partial x_j}\right) + G_\omega - Y_\omega + D_\omega + S_\omega \tag{5}$$

These two equations describe the transport of turbulent kinetic energy k and specific dissipation rate ω. The space coordinate x_i and velocity component $u_i, i = 1, 2, 3$, represent the corresponding variables in the x, y, z directions correspondingly. Γ_k and Γ_ω stand for the effective diffusivity of k and ω, and the term $\widetilde{G}_k$ and G_ω represent the generation of them correspondingly. Y_k and Y_ω are the dissipation caused by turbulence, while source terms are expressed as S_k and S_ω. The cross-diffusion term D_ω is introduced to blend the standard $k-\omega$ and $k-\varepsilon$ models.

The convective terms are discretized using the advection upstream splitting method (AUSM)[44] which utilizes the characteristic speeds from the neighboring cells to evaluate the cell interface Mach number. Subsequently, this value further determines the upwind extrapolation value of the inviscid convective flux.

Mesh	Nx	Ny	Nz	Grid refinement ratio	Total of grid cells	Grid Convergence Index
Coarse	357	20	40	2.3	360000	0.9530%
Fine	447	25	58		830500	
Dense	714	30	67	2.2	1818870	0.7625%

Table 2: Mesh parameters for the grid independence verification and numerical validation.

The method shows the excellent resolution capability for shock discontinuity problems. The density-based implicit solver is employed to enhance computational convergence. The Green-Gauss Node-Based gradient discretization method is used to confirm the nodal values that are constructed from the weighted average of the cell values surrounding the nodes. By solving a constrained minimization problem, this scheme accurately reconstructs nodal values from cell-centered data on meshes while preserving second-order spatial resolution. The discretization of the convection, the turbulent kinetic energy and other terms all employ the second-order upwind scheme to ensure computational accuracy. The fluid medium is regarded as single-specie thermally perfect air. Sutherland's formula is adopted to calculate viscosity.

3.2 Grid independence verification and numerical validation

The experimental model under uncontrolled conditions is employed for grid independence verification and numerical validation. Figure 5 shows the schematic diagram of simplified computational domain and boundary conditions also are marked with different colors. The model consists of two parts: the replaceable nozzle and the isolator test section. In this case, the aspect ratio of the used model is 1, indicating that the flow field exhibits highly spatial. Therefore, the sidewall effect cannot be ignored, and three-dimensional numerical simulation is essential. To conserve computational resources, half of the actual flow domain is selected for meshing and numerical calculations. All grids are structured hexahedral meshes, and the minimum mesh height near the wall surfaces is set to 100 and $50\mu m$. Three types of grids are prepared: coarse, fine and dense. The number of grid cells of the isolator section in different directions is shown in the table 2. The grid refinement ratio between adjacent mesh is set to r = 2.3 and 2.2 according to Roache's recommendation[45]. During the numerical computation process, the nozzle inlet is set as the pressure inlet condition, while the isolator outlet is the pressure outlet. The rest of boundaries except the symmetry plane are no-slip adiabatic wall surfaces. Changes in pressure outlet conditions can affect the flow field characterized by the shock train in the isolator section, corresponding to the plug movement in the experimental facility.

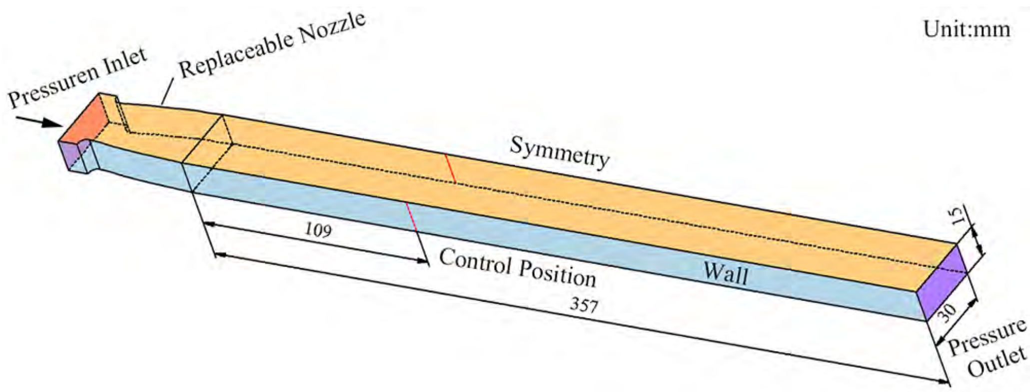

Figure 5: Numerical calculation domain and boundary conditions.

Figure 6 and figure 7 show comparisons of experimental data and numerical results obtained using different resolution grids, including schlieren images and static pressure distributions in the test isolator section. The time-averaged wall pressure p_w is normalized by the incoming static pressure p_0 according to the following formula:

$$PR = \frac{p_w}{p_0} \tag{6}$$

In figure 6, it is shown that numerical simulation accurately predicted the complex flow situation in the isolator, including leading-edge shock waves (i), expansion waves (ii), separation bubbles (iii), reattachment shock waves (iv), reflected shock waves (v), and shear layers (vi), etc. As the grid density increases, the flow structures within the shock train become increasingly distinct. Numerical schlieren results from the three grids are almost consistent, and the primary flow structures in the leading-edge shock wave region are clearly revealed compared with experimental schlieren images.

Numerical simulation has demonstrated its capability for qualitative computation in complex flow fields, but its ability to provide quantitative insights remains to be examined. Figure 7 shows the comparison between the top-wall pressure distribution obtained from numerical simulations using different grids and experimental data collected by pressure transducers, which shows good agreement. Results from the coarse mesh exhibit a slight deviation in the starting position of pressure rise caused by the shock train due to its lower computational resolution. Results show a relative error of 4.72% for the coarse grid compared to merely 1.42% for the fine one. Moreover, a quantitative comparison is performed using the Grid Convergence Index (GCI)[45]. The total pressure recovery coefficient at the exit is selected as the evaluation parameter, and the GCI values for adjacent meshes are presented in table 2. The calculated GCI is below 1%, demonstrating satisfactory convergence across the three grids examined. Therefore, the fine grid is selected for subsequent numerical calculations to comprehensively consider computational accuracy and efficiency. Constrained by the experimental setup, pressure measurements in the leading-edge shock wave region are difficult to perform densely, highlighting the advantage of numerical simulation.

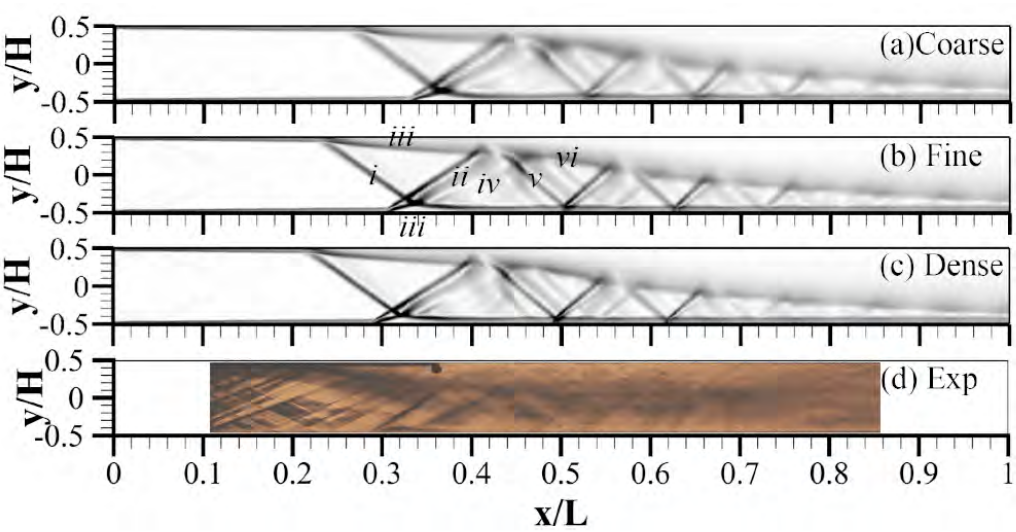

Figure 6: Comparison of experimental and numerical schlieren in the isolator.

4. Results and discussion

The steady-state and dynamic characteristics of the shock train are compared with and without flow control: Based on experimental and numerical results, the influence of different flow control methods on flow field structures in the isolator is investigated; Subsequently, experimental data are used to study the effects of suction and injection on the oscillation characteristics of the shock train.

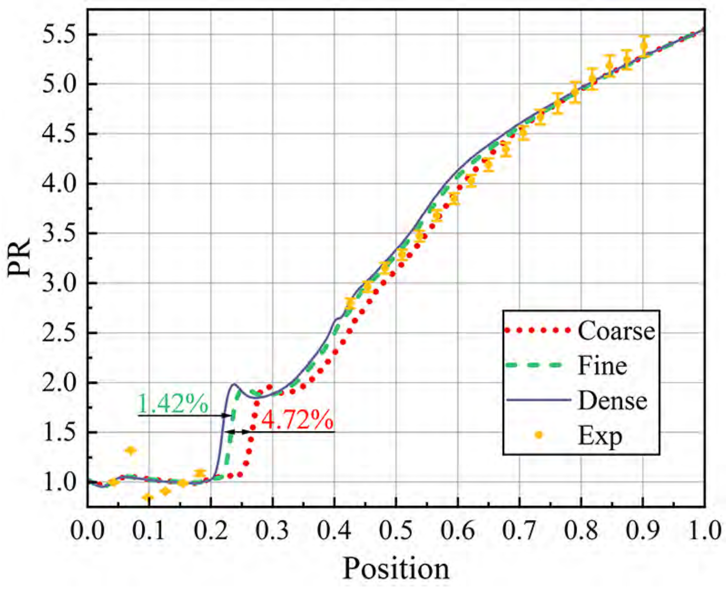

Figure 7: Comparison of experimental and numerical static pressure distributions along the top wall surface in the isolator.

4.1 The baseline flow and intervention-generated perturbations.

In actual experimental environments, background waves might arise due to factors such as the assembly of test facilities. These chaotic waves repeatedly reflect in the isolator, causing spatial inhomogeneity of the flow field. Figure 8 illustrates the flow field structures and pressure distribution under different flow control conditions. These background waves cause fluctuating pressure in the isolator. In the uncontrol case, pressure fluctuations in the isolator are relatively the mildest, indicating the lowest intensity of background waves. When suction and injection control methods are applied, waves are generated at the suction slots and injection slits, and these additional waves increase pressure fluctuations within the flow field. Specifically, during suction experiments, waves generated at both the top and bottom suction slots lead to the most pronounced pressure disturbance.

However, suction and injection exert entirely different effects on pressure distribution near the control position: suction creates a localized low-pressure zone near the slot, thereby forming an adverse pressure gradient region within a limited downstream range; injection generates a regional high-pressure zone near the slit, causing a favorable pressure gradient in the same area. These differing pressure distributions and additional flow field structures could result in changes to shock train behavior.

Figure 9 illustrates the schlieren images and pressure distribution of shock trains forming in the test section when backpressure is applied at the outlet, both with and without flow interventions. The backpressure condition at the outlet for the four selected cases exhibits relatively close, with the leading edge of the shock train all situating near the control position. Under test flow conditions, the backpressure propagates along the boundary layers to a specific location of the isolator, causing the local boundary layer to thicken and form an aerodynamic wedge. Oblique shock waves subsequently are induced from the wall surfaces, who interact and turn into transmitted shock waves that impinge upon the wall. The adverse pressure gradient on the local wall faces a sudden increase, leading to the boundary layer separation. As the transmitted shock waves reflect away from the wall, the boundary layer reattaches and induces a reattachment shock wave. These complex waves repeatedly reflect and interfere in the confined isolator, governing the downstream flow field, who simultaneously decelerates and increases the pressure of the incoming flow.

After implementing flow intervention methods, suction and injection inevitably affect the shock train structure. Fluid suction aims to weaken strong SWBLI by removing the boundary layer. In supersonic

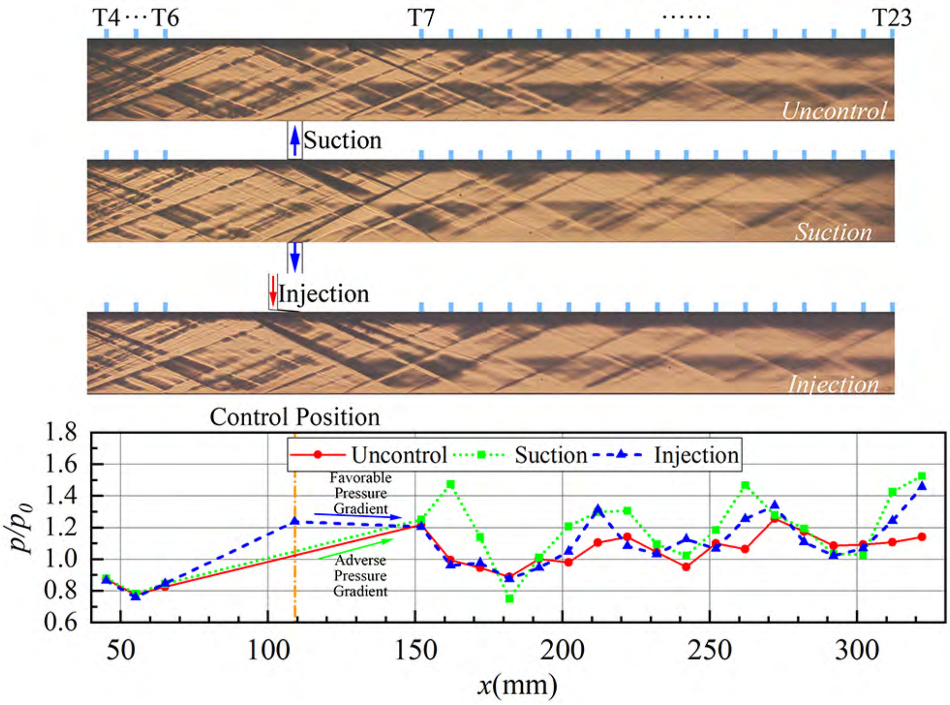

Figure 8: Schlieren images and pressure distribution in the isolator under throughflow conditions.

flow fields, any minor disturbance generates "waves". Consequently, two distinct waves form near the suction slot: the expansion wave at the starting edge of the slot; the compression wave at its ending position. The effects of boundary layer suction on the shock train are as follows: First, by removing the near-wall boundary layer, the redeveloped downstream boundary layer becomes relatively thinner, resulting in a smaller separation structure formed by SWBLI; Second, by eliminating the subsonic flow region near the wall, the upstream propagation of backpressure is blocked, confining its impact on the isolator to the downstream range of the suction slot.

During injection control, nitrogen is injected at a slight angle through the injection slit into the isolator driven by pressure difference, thereby influencing the shock train. The total injection pressure (p_i) is normalized using the static pressure of incoming flow (p_0) according to the following formula:

$$MPR = \frac{p_i}{p_0} \tag{7}$$

MPR is the microjet-to-inflow pressure ratio. To inject fluid into the isolator, the injection pressure should exceed the static pressure at the control position. The high-pressure disturbance at the injection slit propagates upstream and downstream along the boundary layer. The upstream propagating disturbance creates the adverse pressure gradient, while the downstream one forms the favorable pressure gradient in a local area. When the shock train is near this favorable pressure gradient region, the pressure-increasing process is suppressed. Moreover, when high-pressure gas is injected at a small angle, it forms an aerodynamic wedge, thereby inducing a compression wave at the upstream edge of the slit. This wave interacts with the shock train to influence the downstream flow field, such as pre-compressing the incoming flow or merging with the downgoing leading-edge shock wave. When injection control is employed, the appropriate injection pressure is crucial. Simultaneously, the shock train is stabilized downstream of the injection slit within a favorable pressure gradient region to enhance the operational margin of the isolator. When the leading-edge shock train reaches upstream of the injection slit, the microjet and induced vortices continue to enhance momentum exchange within the separation zone. A more practical approach involves implementing a distributed microjet injection, ensuring the leading-edge

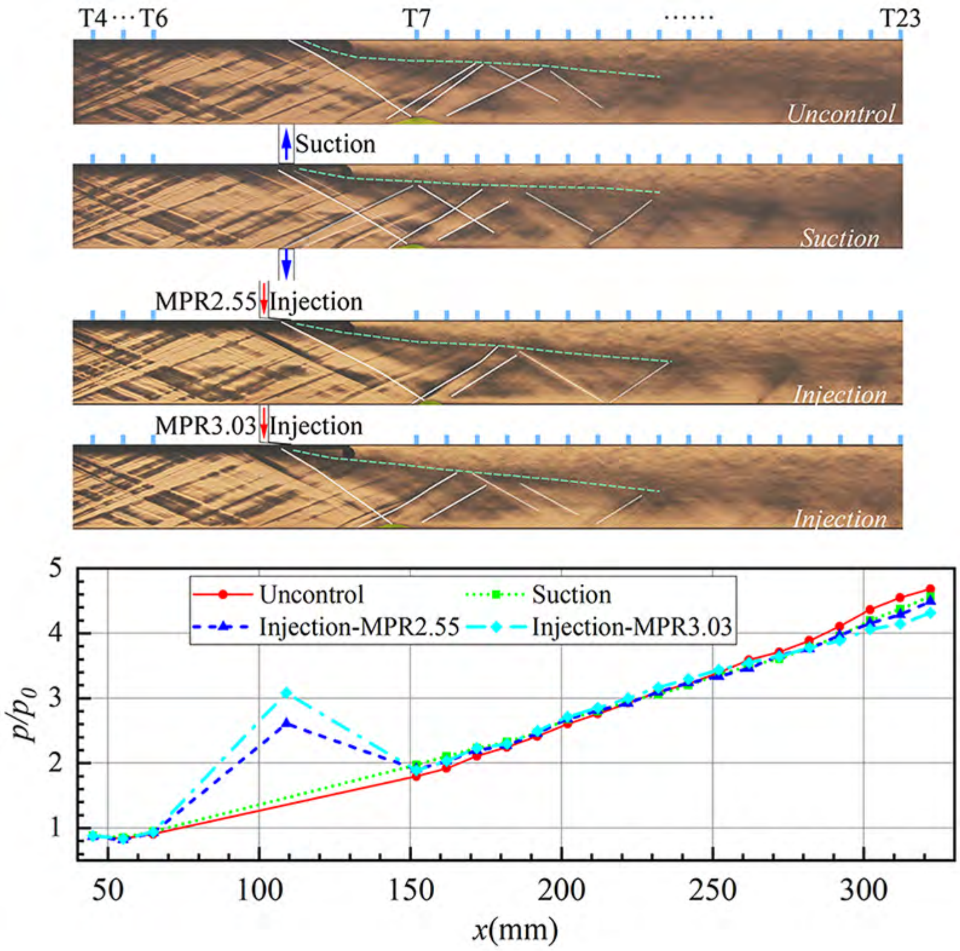

Figure 9: Schlieren images and pressure distribution of shock trains with and without flow intervention methods.

shock train remains near the injection slit.

4.2 Flow field response and three-dimensional structural evolution.

In section 4.1, based on schlieren images and pressure data, some understanding of the flow field environment in the isolator under different flow control methods is gained. However, these data are planar or linear, insufficient to deepen our comprehension of these fields. Within a highly confined space like the isolator, the flow exhibits significant three-dimensional characteristics. Therefore, numerical simulation results are essential to complement the investigation of flow field structures under various flow control methods.

Within the isolator, shock waves and separation bubbles interact through the complex coupling mechanism, resulting in highly intricate flow field structures. The influence of separation bubbles on the flow field is critical: The subsonic flow within the separation bubbles provides a pathway for the upstream propagation of backpressure, linking the exit condition with the shock train leading edge; Simultaneously, the size of the separation bubble is influenced by the shock intensity, and separation zones deteriorate the isolator performance by reducing the flow quality at the exit. Figure 10 displays the skin friction lines on the top, side, and bottom wall surfaces in four numerical cases, with corresponding experimental schlieren images shown for comparison. For clarity of visualization, the top, side, and bottom walls of the isolator are unwrapped and laid flat, with their specific spatial relationships illustrated in figure 10(e). Skin friction lines clearly reveal the flow patterns on the wall surface. When combined with the shock wave structures visualized by schlieren images, they facilitate a comprehensive understanding of the three-dimensional flow field in the isolator. The numerical calculation condition at the exit is that the backpressure ratio equals 5.5, at which point the shock train leading edge is located near the control position and slightly upstream. Under these conditions, various flow control configurations are implemented, and the internal flow field of the isolator responds accordingly, thereby enabling a direct comparative investigation of their control mechanisms.

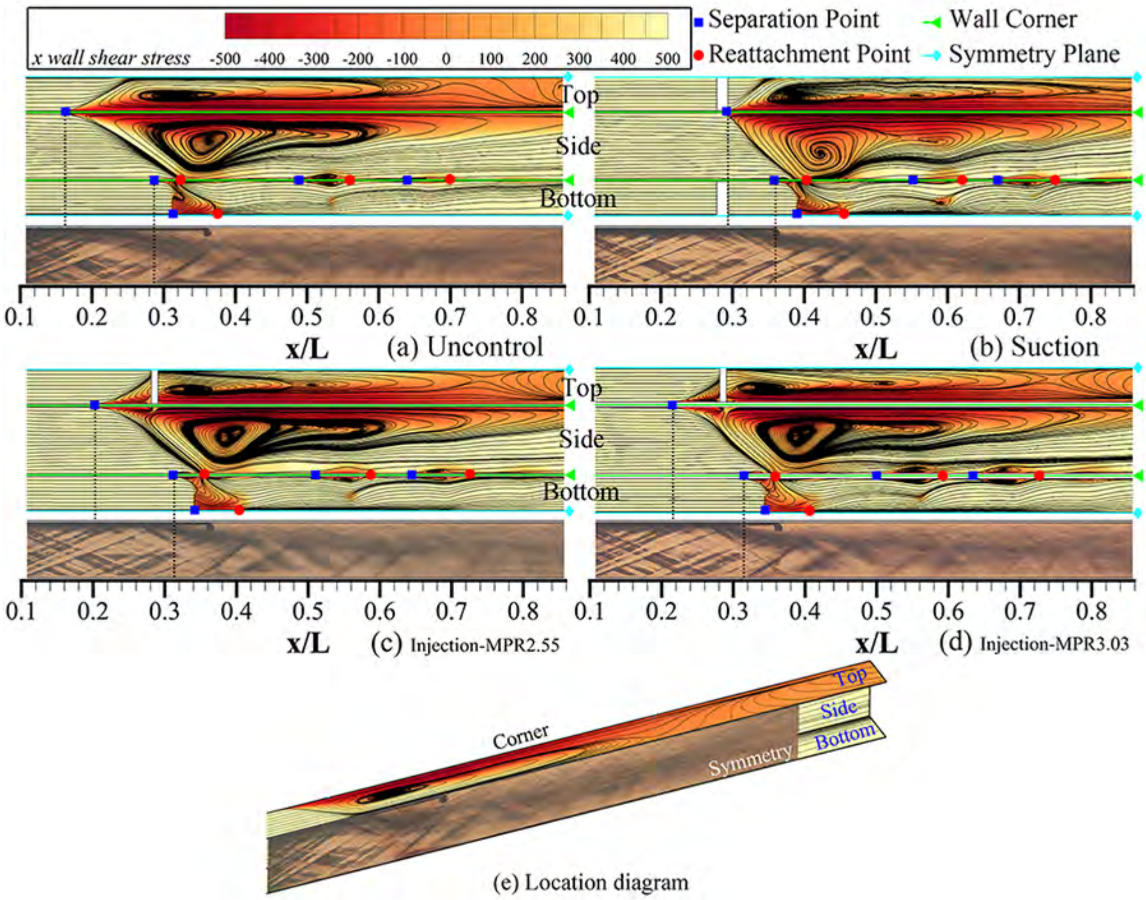

Figure 10: Wall separation patterns of the top wall, the side wall and the bottom wall in numerical cases, illustrated by skin friction lines and the x wall shear stress. And schlieren images in four experimental cases.

As observed in figure 10, the oblique shock train in the isolator exhibits asymmetric pattern, with the shock wave structure biased towards one side. In this case, the shock train is deflected towards the bottom wall, manifesting as a large separation region that forms in the top wall corner and fails to reattach. Conversely, small separation regions are established on the bottom wall, where multiple small separation bubbles develop in the corner due to the repeated reflection of waves. The thicker boundary layer in the corner is more susceptible to backpressure, indicating that the separation point here is located more upstream compared to that on the symmetrical plane. Hence, in experimental schlieren images, the observed separation or shock initiation points on the top and bottom walls may lie slightly downstream of the separation points identified in numerical simulations.

Different flow intervention methods exert distinct effects on wall separation patterns. During suction control, the shock train leading edge becomes anchored at the slot edge due to the fluid removal, when the separation bubble reaches the slot location. In contrast, the microjet injection shows a more subtle influence on the flow field; nevertheless, it still achieves beneficial effects. For a more quantitative comparison of different control methods, table 3 summarizes the separation point locations on the bottom symmetry plane and the corresponding mass flow rate changes in four cases. Suction has a relatively significant effect on the shock train, shifting its leading edge downstream by 7.62%L—this is achieved at

Flow interventions	Separation-point locations on the bottom symmetry plane	Mass flow rate changes (%)
Uncontrol	0.3141	0
Suction	0.3903	-0.9257
Injection-MPR2.55	0.3411	+0.1949
Injection-MPR3.03	0.3438	+0.3280

Table 3: The comparison of the separation-point locations and mass flow rate changes.

$\bar{D}$	PR4.5	PR5.0	PR5.5
Uncontrol	1.2984	1.3250	1.3213
Suction	1.2921	1.3084	1.2910
Injection-MPR2.55	1.2980	1.3359	1.2985
Injection-MPR3.03	1.2912	1.3278	1.2940

Table 4: Total pressure distortion index under various backpressure ratio conditions.

the cost of removing 0.9257% of the main flow rate. In contrast, injection at MPR 2.55 shifts the leading edge downstream by 2.70%L, with the injection flow rate accounting for only 0.1949% of the main flow. When MPR is increased to 3.03, the associated rise in injection flow rate leads to a slight enhancement in control capability.

As the backpressure increases and the shock train moves upstream, its structure becomes progressively asymmetric—this phenomenon is particularly evident in oblique shock trains. It undoubtedly affects the exit flow quality, thereby influencing the combustion performance. To investigate this effect, numerical results for aforementioned configurations are compared at exit backpressure ratios of 4.5, 5.0, and 5.5. Figure 11 presents the distribution of the total pressure recovery coefficient on the outlet cross-section. When the backpressure ratio is relatively low (4.5), the leading-edge shock train is located at approximately 220 mm. At this point, the leading edge is situated far from the control position, resulting in limited flow control effectiveness and minimal changes in the outlet flow. As the backpressure increases, the shock train gradually approaches the control region. The accompanying structural changes in the shock train induce corresponding alterations in the exit flow conditions. Total pressure distortion index $\bar{D}$ is used to quantitatively compare the outlet flow quality and the formula is as follows:

$$\bar{D} = \frac{(p_e)_{max} - (p_e)_{min}}{(p_e)_{qa}} \tag{8}$$

The subscripts max, min, and qa denote the maximum, minimum, and mass-flow-rate-averaged values, respectively. This is a commonly used metric for quantifying the degree of flow field distortion. As confirmed in table 4, both suction and injection effectively reduce flow distortion and enhance flow quality at the isolator exit when the shock train is within the control region. Conversely, the control effect becomes insignificant when the shock train is located far from the control position. This indicates that the relative position between the control region and the shock train is a key factor determining control effectiveness.

Based on the preceding analysis, the coupling mechanism between the waves and the wall separation zones is identified as the critical element governing the shock train structure. Accordingly, the three-dimensional flow field structure inside the isolator is visualized in figure 12, where the waves are represented by iso-surfaces calculated using the following formula:

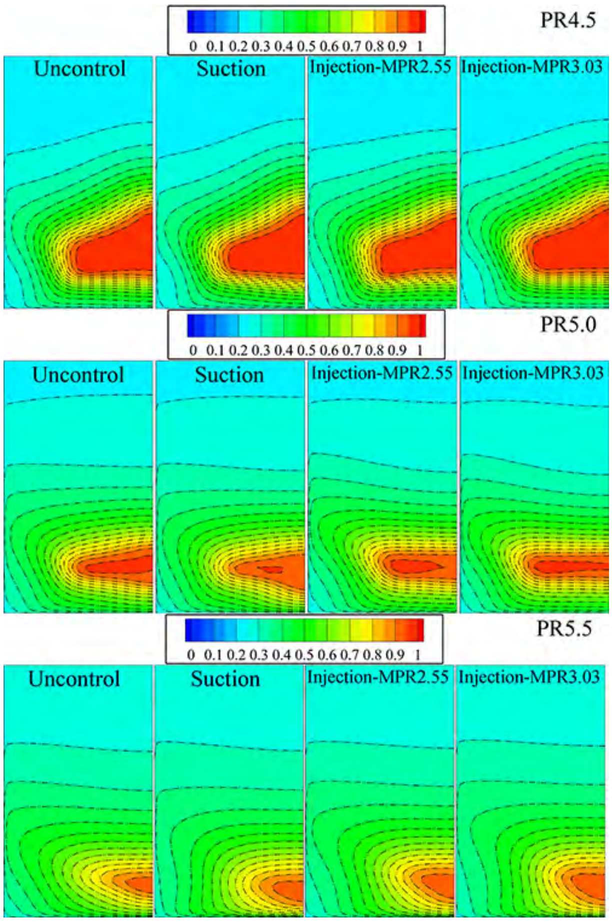

Figure 11: Contours of total pressure recovery coefficient at outlet under different backpressure ratio conditions.

$$\frac{\partial \rho}{\partial x} = \pm 100 \tag{9}$$

The positive density gradient signifies flow governed by compressive shock waves, whereas the negative value indicates influence from expansion waves. It can be observed that the flow in the shock train region is alternately affected by compression and expansion, exhibiting considerable complexity. Under the influence of backpressure, boundary layer separation occurs, inducing the formation of shock waves. Expansion waves promote the contraction of the separation zone, while the shock waves undergo repeated reflections within the isolator. As a result of these interactions, the corner separation bubbles diminish in a fluctuating manner along the flow direction, which is reflected by the fluctuation of shear stress lines on the side wall in figure 10. The separation bubble on the top wall does not affect the vicinity of the symmetry plane and exhibits a more extensive streamwise development, which explains the absence of both separation and reattachment points on the top-wall centerline in figure 10. In contrast, the separation bubble on the bottom wall intrudes into the center plane but promptly reattaches.

Under these two intervention methods, the wave system near the slot is directly opposite: in the suction case, the flow first undergoes an expansion wave followed by a compression wave; during injection control, the sequence is a compression wave preceding an expansion wave. This contrasting behavior is consistent with the distinct effects that each intervention method exerts on the flow channel. This helps us understand the characteristics of different flow intervention methods.

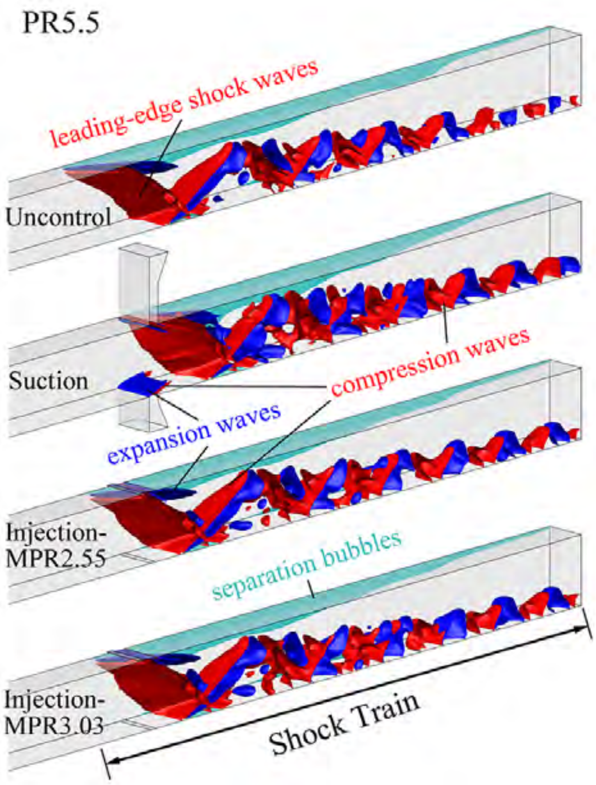

Figure 12: The three-dimensional flow field structure in the isolator.

4.3 Gains from flow intervention on self-excited oscillations.

To investigate the self-excited oscillation characteristics of the shock train under different flow control methods, experimental data obtained under the fixed-plug configuration are compared. Figure 13 - figure 16 present selected continuous schlieren images within 0.01 seconds, along with the mean pressure values and oscillation ranges in a 1-second duration across four cases. The time-series data of gray values from the bottom-wall schlieren images are extracted and processed to quantitatively compare the self-excited oscillation characteristics of the shock train. Detailed processing instructions are mentioned in the Reference[15]. The shock train induces pressure oscillations within the isolator. While the pressure upstream of the shock train remains relatively stable, the oscillation amplitude gradually increases toward its downstream region. Even under constant backpressure conditions, the shock train oscillation still occurs. This phenomenon is closely related to the inherent instability associated with shock waves, boundary layers, and separation bubbles. As evident from schlieren images, the upgoing leading-edge shock wave exhibit significant movement along the bottom wall surface. Spectrum diagrams provide a relatively quantitative representation of the oscillation characteristics of the leading-edge shock foot under different flow intervention methods. Regarding the oscillation range, suction reduces the self-excited oscillation range compared to the uncontrol case, while injection does not demonstrate a significant gain. Suction and injection both induce the compression waves, yet neither exhibit similar capabilities in suppressing self-excited oscillations. This indicates that the leading-edge separation bubble is the primary factor influencing self-excited oscillation characteristics: suction achieves oscillation suppression by partially removing the near-wall separation region, whereas injection introduces additional instability factors into the separation region and thus fails to achieve the desired positive gain.

Power spectral density (PSD) analysis is used to study the real-time spectral characteristic of the shock train in these experiments. Pressure data from T6, T7, T13, T19, and T24 are processed into PSD contours for comparison in uncontrol, suction and MPR3.03 injection cases, as shown in figure 17. T6, located upstream of the leading-edge shock train, suction and injection reduce pressure disturbances within the

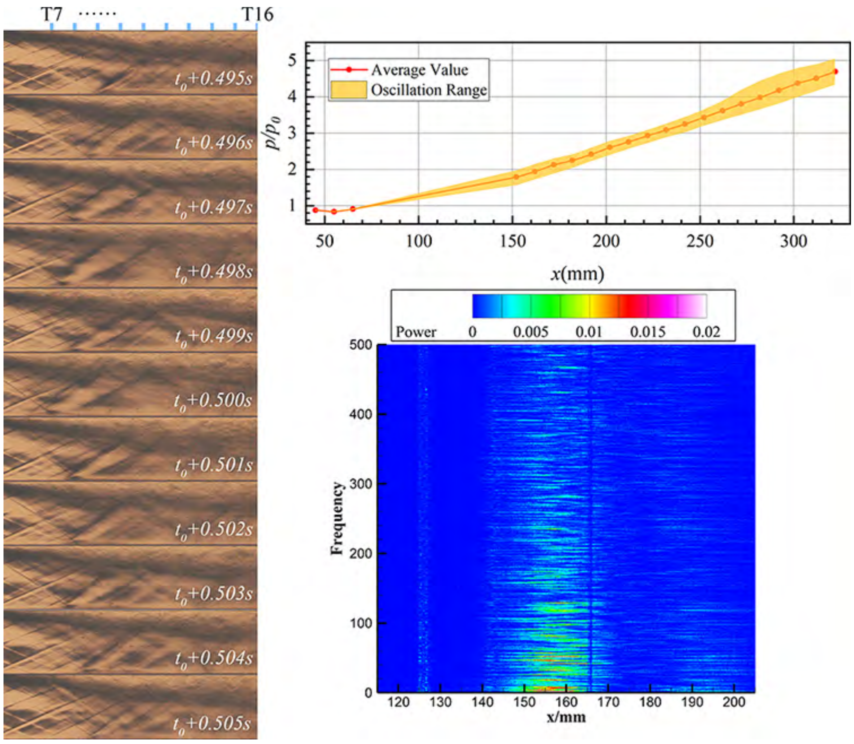

Figure 13: Schlieren images of self-excited oscillations, streamwise pressure distribution, and spectrum diagram of the leading-edge shock wave oscillation without flow control methods.

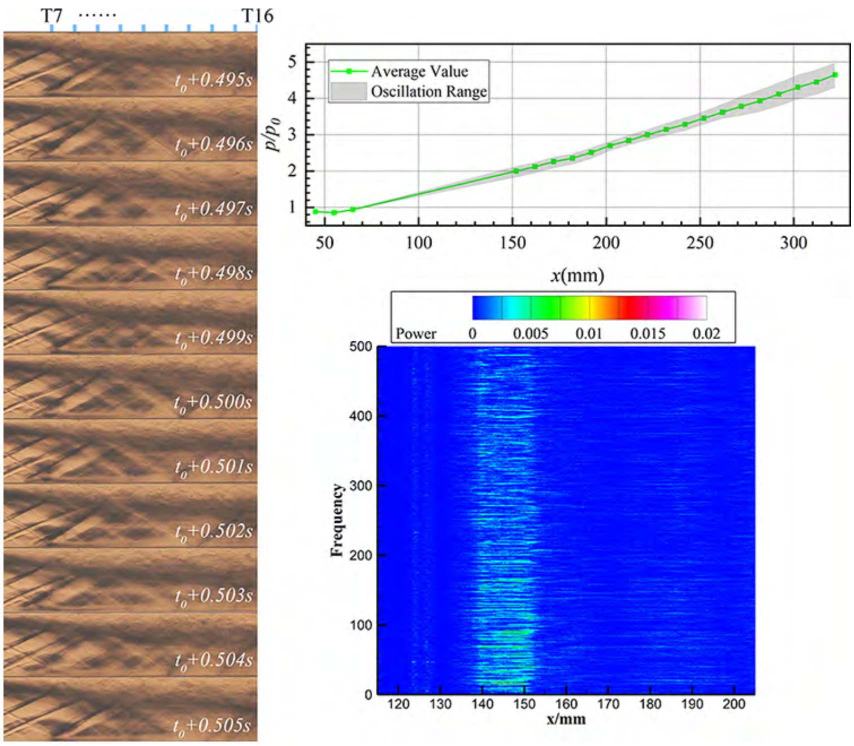

Figure 14: Schlieren images of self-excited oscillations, streamwise pressure distribution, and spectrum diagram of the leading-edge shock wave oscillation with suction control.

boundary layers compared to the uncontrol case. T7 is situated at the leading-edge shock train position, where intervention methods slightly enhance the oscillation intensity in the approximate range of 30-40 Hz. T13 lies downstream of the leading-edge shock train, where pressure oscillations are suppressed by

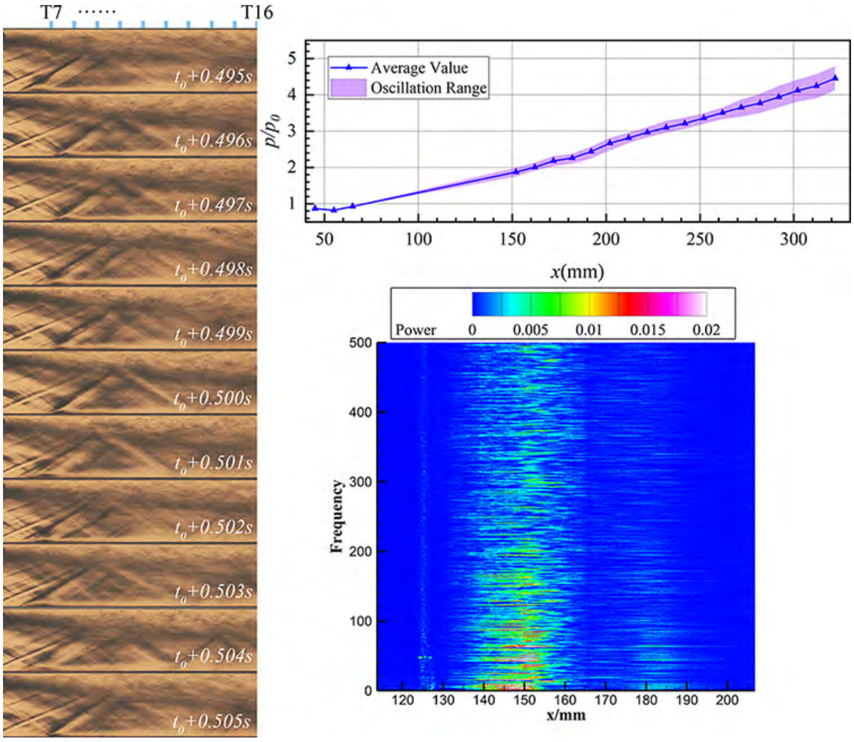

Figure 15: Schlieren images of self-excited oscillations, streamwise pressure distribution, and spectrum diagram of the leading-edge shock wave oscillation with MPR2.55 injection control.

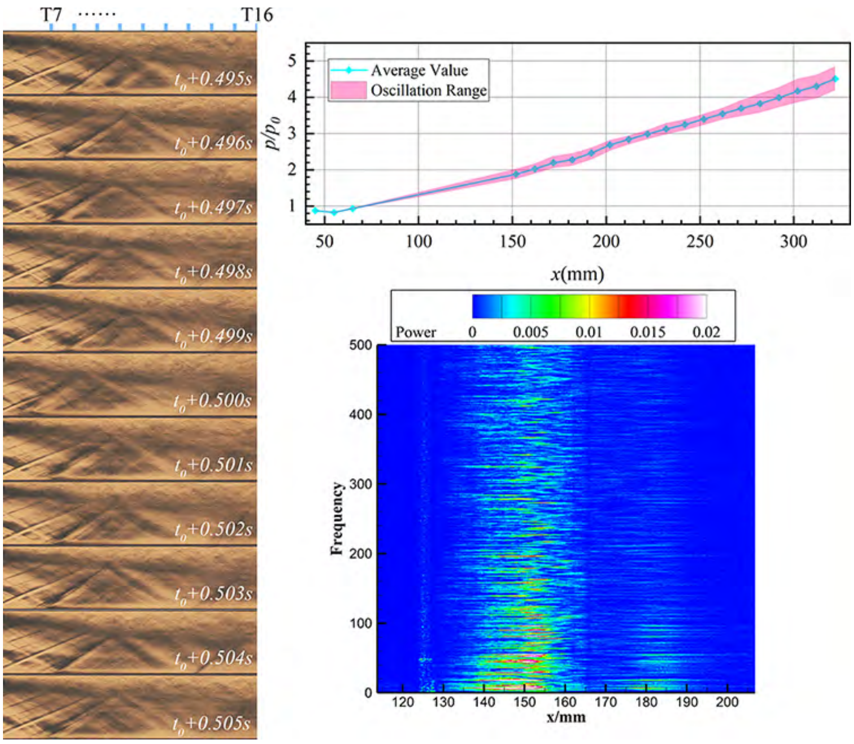

Figure 16: Schlieren images of self-excited oscillations, streamwise pressure distribution, and spectrum diagram of the leading-edge shock wave oscillation with MPR3.03 injection control.

two flow control methods, particularly at frequencies below 30 Hz. T19 and T24 are located downstream of the shock train and near the isolator exit, respectively. Due to their considerable distance from the control position, the influence of flow intervention measures is relatively limited. Consequently, it can be observed that suction and injection alter the top-wall pressure fluctuations. Flow control methods cause pressure disturbances to concentrate in the leading-edge shock train region, that is, near the control position.

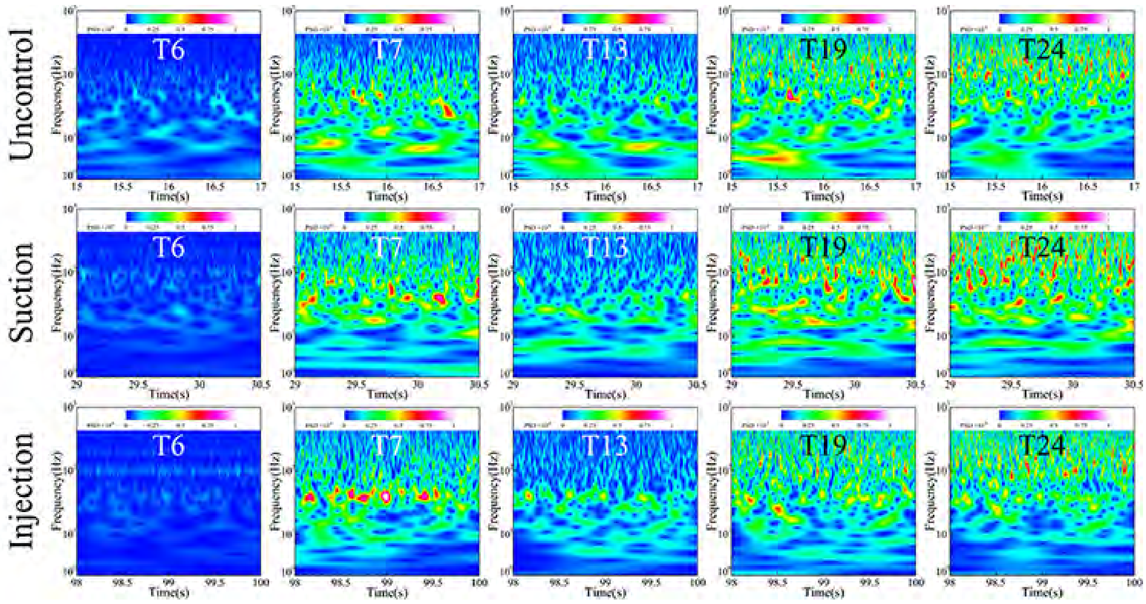

Figure 17: PSD contours of pressure signals at T6, T7, T13, T19, and T24 in three cases.

4.4 Spatial dynamics of the modulated shock train.

Dynamic Mode Decomposition (DMD) is employed to analyze the self-excited oscillation structure of the shock train. 1000 experimental snapshots of the self-excited oscillation process with a duration of 1 second are selected for analysis. Figure 18(a) illustrates the relationship between cumulative energy and the rank in the DMD analysis. For the self-excited oscillation, the steady-state component represented by Rank=0 accounts for over 99% of the total energy. The proportions of steady-state energy in different cases are also shown in the figure. It can be observed that the steady state energy share of the shock train increases by 0.12% under suction control, whereas it decreases by 0.35% and 0.38% respectively in two injection cases. This further confirms that suction enhances the stability of the shock train, while injection increases the fluctuation of the flow field (related to vortices induced by the microjet promoting momentum exchange). In the DMD analysis, Mode 0 corresponds to an eigenfrequency of 0, representing the steady mean flow field. Therefore, figure 18(b) compares the energy distribution among different modes in the remaining oscillation energy. The self-excited oscillation energy of the shock train is primarily distributed in the first few modes, with both suction and injection resulting in a relatively more balanced distribution of oscillation energy. When the mode number exceeds 4, the energy contribution of a single mode falls below 0.02%.

Thus, the four modes with the highest oscillation energy (Mode 1, Mode 2, Mode 3 and Mode 4) are used to analyze the unsteady oscillation structure of the shock train, as shown in figure 19 - figure 22, with the steady modes also presented for comparison. Consistent with the previous analysis, the steady-state flow field exhibits relatively higher energy during uncontrol and suction cases, resulting in greater intensity in the flow field image corresponding to Mode 0. Furthermore, the frequency/energy ratio figures show two distinct peaks: one in the approximate range of 131–139 Hz and the other between 360–393 Hz. Across different cases, the energy peaks fall into varying frequency bands. In the cases of uncontrol, suction, and injection-MPR3.03, the dominant modal frequencies consistently lie in the high-frequency range, though with varying specific values of the energy ratio. A notable exception is the injection-MPR2.55 case, when the dominant modal frequency falls in the low-frequency range, and the peak energy intensity in the high-frequency range is significantly suppressed. Additionally, near the lower frequency of 27

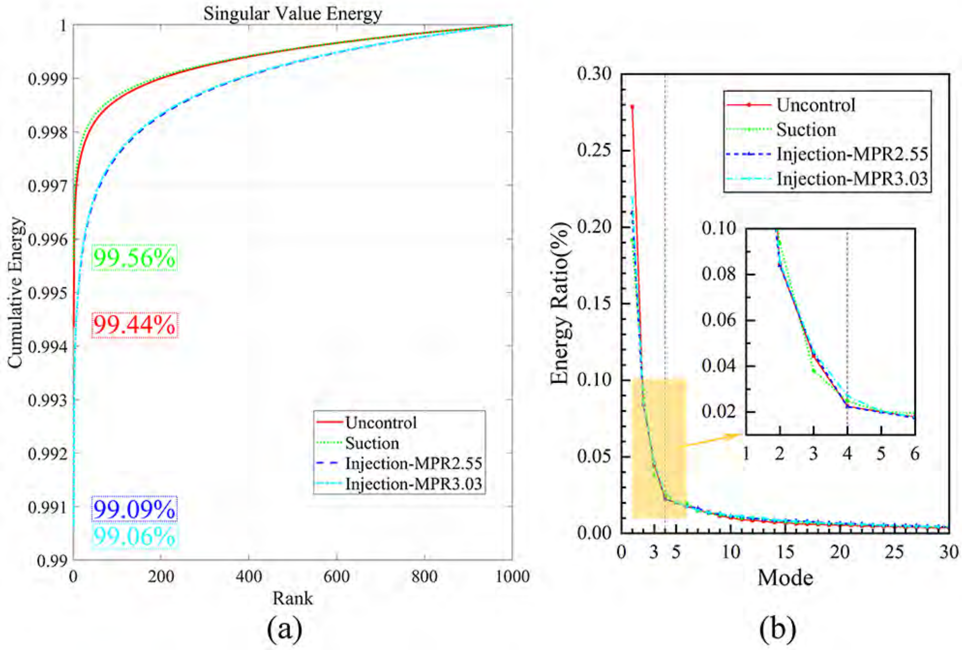

Figure 18: The distribution of steady-state and oscillatory energy in four cases. (a) The relationship between cumulative energy and the rank in the DMD analysis. (b) The oscillation energy distribution among different modes.

Hz, moderate modal energy is distributed sparsely. Based on the flow field diagrams of different modes, it is observed that the self-excited oscillation intensity of the shock train is predominantly concentrated in the leading-edge region: it includes areas near the downward incident shock, the upward reflected shock, and the reattachment shock (This is due to the downward deflection of the shock train in present cases, resulting in higher intensity of the downward oblique shock). The background shock system also exhibits a certain impact. The intensity distributions of Mode 1 and Mode 2 are predominantly clustered near the two incident shocks and the transmitted shocks of the leading-edge shock train. Furthermore, those of Mode 3 and Mode 4 are primarily distributed around the subsequent reflected shocks and the reattachment shock. Therefore, different flow intervention methods enhance the intensity concentration in the leading-edge region in the present experimental configuration due to the merging of the generated waves with the leading-edge shock wave. This demonstrates that different flow control methods exert distinct influences on the oscillation characteristics of the shock train flow field. This is related to the effects of intervention methods on flow field structures, such as separation bubbles and wave structures, and requires in-depth investigation.

In section 4.3, the spectral analysis of top-wall pressure data reveals the oscillation behavior of the large separation zone here. This is attributed to the fact that the backpressure influence extends to the control position during the self-excited oscillation experiments and all downstream pressure transducers are situated within the separation zone induced by the shocks. In this section, DMD analysis based on schlieren images captures the spatial distribution of wave intensity. Compared to shock oscillation, the separation-bubble oscillation is relatively lower in frequency. The oscillation characteristics of both the separation zone and the shock structure together contribute to a comprehensive understanding of the self-excited oscillation.

5. Conclusion

This study demonstrates that suction and injection are effective yet distinct methods for modulating the shock train in an isolator, primarily through their disparate impacts on the flow field. The main

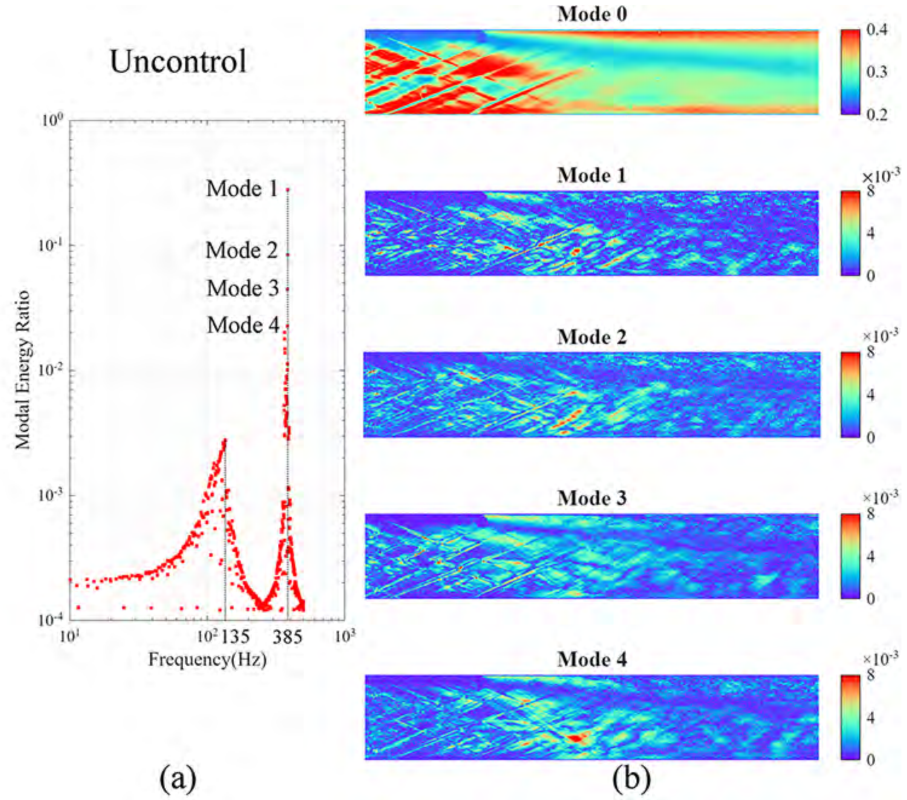

Figure 19: (a) The relationship between energy ratio and frequency of DMD mode. (b) The shock train flow field of the first 5 modes in the uncontrol case.

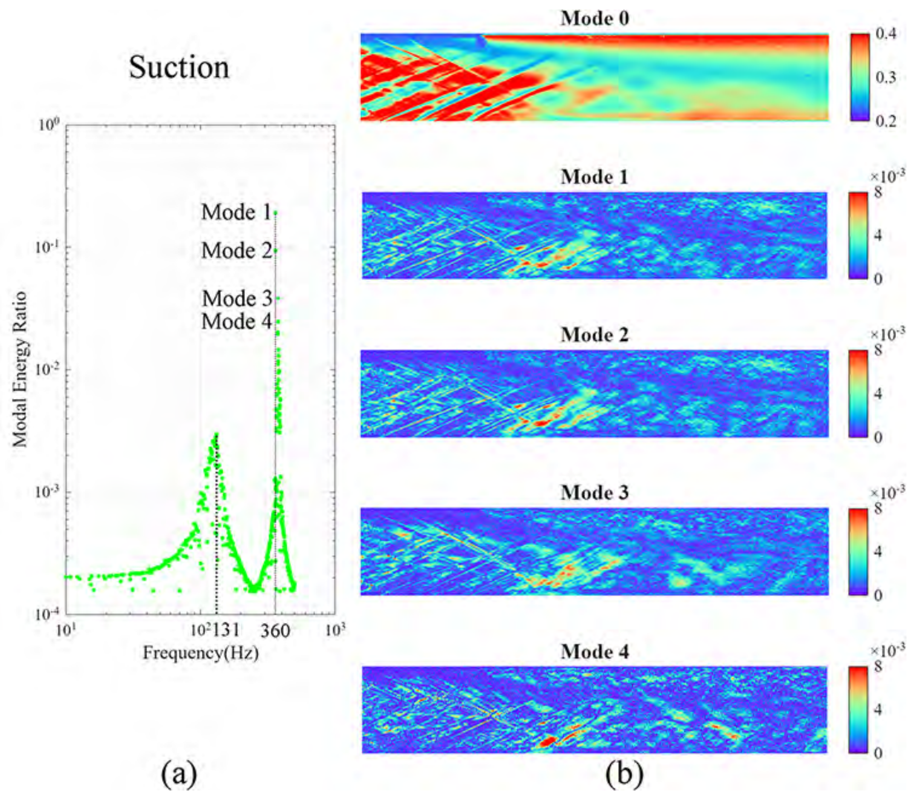

Figure 20: (a) The relationship between energy ratio and frequency of DMD mode. (b) The shock train flow field of the first 5 modes in the suction case.

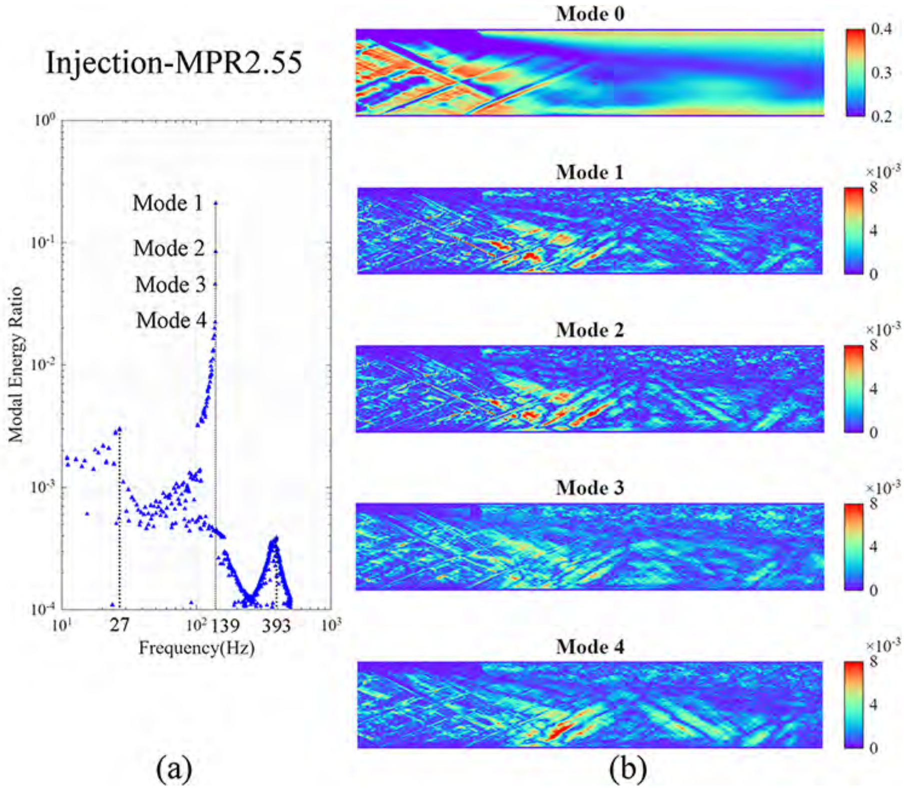

Figure 21: (a) The relationship between energy ratio and frequency of DMD mode. (b) The shock train flow field of the first 5 modes in the injection-MPR2.55 case.

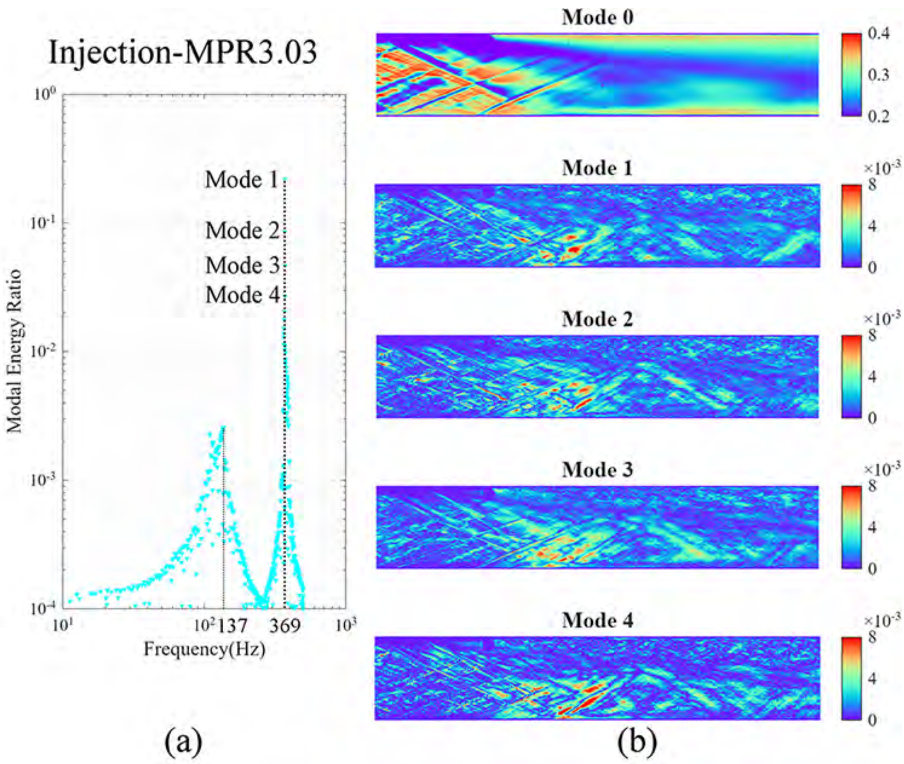

Figure 22: (a) The relationship between energy ratio and frequency of DMD mode. (b) The shock train flow field of the first 5 modes in the injection-MPR3.03 case.

conclusions are as follows:

1. Suction creates a localized low-pressure zone and removes the near-wall boundary layer. This thins the downstream boundary layer, suppresses separation, and blocks the upstream propagation of backpressure, thereby anchoring the shock train and shifting it downstream by 7.62%L under certain conditions. In contrast, microjet injection creates a favorable pressure gradient and enhances momentum exchange that results in a smaller downstream shift (2.70%L) in research cases.

2. The leading-edge separation bubble is the dominant factor influencing the self-excited oscillation. Suction effectively suppresses self-excited oscillations by removing part of the separation bubble, enhancing overall stability. Injection, however, introduces unsteadiness, thereby slightly increasing flow field fluctuations. They both cause fluctuations to concentrate in the leading-edge shock train region. The oscillation frequency of the separation bubble (30-40Hz) is lower than that of the shock wave (360-393Hz, 131-139Hz), and understanding both is crucial for a comprehensive view of the oscillation phenomenon.

3. The separation structure within the shock train is asymmetric. This is due to the larger separation bubble on one side exhibits a more extensive streamwise development, while the smaller separation bubble on the opposite side primarily develops in the spanwise direction. Both intervention methods can reduce flow distortion and improve flow quality at the isolator exit when the shock train is near the control position.

The choice of intervention method involves a trade-off. Suction offers simplicity and enhanced stability but incurs mass flow loss. Injection preserves captured mass flow and allows for precise control but adds structural complexity and flow unsteadiness.

Furthermore, both suction and injection can be deployed in arrayed configurations to expand their applicability. The influence of pulsed microjet injection on shock train oscillation characteristics also presents a potential avenue for research.

Acknowledgements

The present research work is financially supported by the National Natural Science Foundation of China (Grant No. 52272405), and the Key Research and Development Program of Shaanxi Province (Program No. 2023ZY1-JCYJ-01-01).

The authors also gratefully acknowledge financial support from China Scholarship Council.

6. Declaration of interests

The authors report no conflict of interest.

References

[1] Kazuyasu Matsuo, Yoshiaki Miyazato, and Heuy-Dong Kim. Shock train and pseudo-shock phenomena in internal gas flows. *Progress in aerospace sciences*, 35(1):33–100, 1999.

[2] Yubao He, Juntao Chang, Wen Bao, Hongyan Huang, and Daren Yu. Numerical investigation of local resistance to backpressure in hypersonic inlet with suction. *Journal of Propulsion and Power*, 32(6):1531–1543, 2016.

[3] Julian Giehler, Thibault Leudiere, Robert Soares Morgadinho, Pierre Grenson, and Reynald Bur. Experimental and numerical investigation of porous bleed control for supersonic/subsonic flows, and shock-wave/boundary-layer interactions. *Aerospace Science and Technology*, 147:109062, 2024.

[4] Huang Hexia, Tan Huijun, Sun Shu, and Ning Le. A fluidic control method of shock train in hypersonic inlet/isolator. In *50th AIAA/ASME/SAE/ASEE Joint Propulsion Conference*, page 3846, 2014.

[5] Ziao Wang, Kejing Xu, and Juntao Chang. Distributed fluidic control method for alleviating rapid movement of shock train. *AIAA Journal*, 60(11):6252–6269, 2022.

[6] Vignesh Ram Petha Sethuraman, Yosheph Yang, and Jae Gang Kim. Interaction of shock train with cavity shear layer in a scramjet isolator. *Physics of Fluids*, 35(3), 2023.

[7] Ziao Wang, Juntao Chang, Chen Kong, and Yunfei Li. Micro-ramp control for shock train structure and oscillation. *AIAA Journal*, 59(12):4881–4904, 2021.

[8] Argyris G. Panaras and Frank K. Lu. Micro-vortex generators for shock wave/boundary layer interactions. *Progress in Aerospace Sciences*, 74:16–47, 2015.

[9] Neil Titchener and Holger Babinsky. A review of the use of vortex generators for mitigating shock-induced separation. *Shock Waves*, 25(5):473–494, 2015.

[10] Deepak Prem Ramaswamy and Anne-Marie Schreyer. Separation control with elliptical air-jet vortex generators. *EXPERIMENTS IN FLUIDS*, 64(5), 2023.

[11] Jinlong Wang, Kaijie He, Qingchun Zhou, and Jinli Wang. Numerical investigation of low-frequency shock train oscillations in a divergent isolator with vortex generator jets. *PLOS ONE*, 20(7):e0328630, 2025.

[12] Yuhui Wang, Fuhao Chen, Zhaoyang Tian, Anxiang Fu, Yao Yao, and Lei Shi. Shock train stabilization by a high-speed jet injection in an inlet isolator of a ramjet engine. *Physics of Fluids*, 37(6), 2025.

[13] Victor V Kuzenov, Sergei V Ryzhkov, and Aleksey Yu Varaksin. Computational and experimental modeling in magnetoplasma aerodynamics and high-speed gas and plasma flows (a review). *Aerospace*, 10(8):662, 2023.

[14] Hesen Yang, Hua Liang, Bo Yang, Haohua Zong, Jinping Li, Dongsheng Zhang, Youde Xiong, Yun Wu, and Yinghong Li. Experimental study on the hypersonic double incident shock wave/boundary layer interaction regulated by plasma actuation array. *PHYSICS OF FLUIDS*, 36(6), 2024.

[15] Fuhao Chen, Zhaoyang Tian, Chengzhi Zhang, and Lei Shi. Experimental investigation of shock train oscillation suppression by a plasma jet in a supersonic isolator. *Experimental Thermal and Fluid Science*, 163:111428, 2025.

[16] Yan Zhou, Zhenbing Luo, Lin Wang, Zhixun Xia, Tianxiang Gao, Wei Xie, Xiong Deng, Wenqiang Peng, and Pan Cheng. Plasma synthetic jet actuator for flow control: Review (in chinese). *Acta Aeronautica et Astronautica Sinica*, 43(03):98–140, 2022.

[17] Amrita Pathak, Pranjal Khare, and Vinayak Kulkarni. Impact of energy deposition as active flow control on scramjet inlet performance using immersed boundary method. *Acta Astronautica*, 224:291–308, 2024.

[18] Ziyu Wu, Xianggeng Wei, Huanhuan Wang, and Junhua Zhang. Application of shape memory alloy in adjustable inlet and nozzle systems (in chinese). *Aerospace Technology*, No.464(02):64–77, 2025.

[19] Yuhui Wang, Junhua Zhang, Zhaoyang Tian, and Lei Shi. Freejet tests on a variable geometry supersonic inlet driven by shape memory alloys. *Journal of Physics: Conference Series*, 3041(1):012007, 2025.

[20] Ziao Wang, Juntao Chang, Yiming Li, Ruoyu Chen, Wenxin Hou, Jifeng Guo, and Lianjie Yue. Oscillation of the shock train under synchronous variation of incoming mach number and backpressure. *Physics of Fluids*, 34(4):046104, 2022.

[21] Nan Li. Response of shock train to fluctuating angle of attack in a scramjet inlet-isolator. *Acta Astronautica*, 190:430–443, 2022.

[22] Wenxin Hou, Juntao Chang, Ziao Wang, Youyin Wang, and Wen Bao. Shock train behavior affected by continuous mach number variation of incoming flow. *Acta Astronautica*, 177:652–665, 2020.

[23] Wenxin Hou, Juntao Chang, Zongqi Xie, Youyin Wang, Linke Wu, and Wen Bao. Behavior and flow mechanism of shock train self-excited oscillation influenced by background waves. *Acta Astronautica*, 166:29–40, 2020.

[24] Wen Shi, Juntao Chang, Junlong Zhang, Jicheng Ma, Ziao Wang, and Wen Bao. Numerical investigation on the forced oscillation of shock train in hypersonic inlet with translating cowl.

Aerospace Science and Technology, 87:311–322, 2019.

[25] Longsheng Xue, Chuan Cheng, Chengpeng Wang, Lantian Zhang, Kang Li, and Keming Cheng. Oblique shock train motion based on schlieren image processing. *Chinese Journal of Aeronautics*, 36(3):30–41, 2023.

[26] Louis M Edelman and Mirko Gamba. Structure of a mach 2 shock train from experimental measurements. In *AIAA Scitech 2020 Forum*, page 1609, 2020.

[27] Gang Liang, Hexia Huang, Huijun Tan, Zhongqi Luo, Xuebin Tang, Canmin Li, and Jia Cai. Shock train/glancing shock/boundary layer interaction in a curved isolator with sidewall contraction. *Physics of Fluids*, 34(11):116106, 2022.

[28] Wei Huang, Han Wu, Yanguang Yang, Li Yan, and Shibin Li. Recent advances in the shock wave/boundary layer interaction and its control in internal and external flows. *Acta Astronautica*, 174:103–122, 2020.

[29] HJ Tan, S Sun, and HX Huang. Behavior of shock trains in a hypersonic inlet/isolator model with complex background waves. *Experiments in fluids*, 53(6):1647–1661, 2012.

[30] Hexia Huang, Huijun Tan, Fangbo Li, Xuebin Tang, Yuan Qin, Libin Xie, Yaoyu Xu, Canmin Li, Simin Gao, Yue Zhang, Shu Sun, and Dan Zhao. A review of the shock-dominated flow in a hypersonic inlet/isolator. *Progress in Aerospace Sciences*, 143:100952, 2023.

[31] Ziao Wang, Juntao Chang, Guangwei Wu, and Daren Yu. Experimental investigation of shock train behavior in a supersonic isolator. *Physics of Fluids*, 33(4):046103, 2021.

[32] Ziao Wang, Juntao Chang, Wenxin Hou, and Daren Yu. Propagation of shock-wave/boundary-layer interaction unsteadiness in attached and separated flows. *AIP Advances*, 10(10):105011, 2020.

[33] Ziao Wang, Renzhe Huang, Yiming Li, Jialin Zheng, Jifeng Guo, and Juntao Chang. Experimental and numerical simulation of shock train characteristics in an isolator with incident shocks. *Aerospace Science and Technology*, 138:108309, 2023.

[34] Dayi Wang, Ziao Wang, Juntao Chang, Renzhe Huang, and Xuanan Xin. Experimental study on dynamic characteristics of shock train in an isolator with different types of incident shocks. *Physics of Fluids*, 36(7):076108, 07 2024.

[35] Nan Li, Juntao Chang, Kejing Xu, Daren Yu, and Wen Bao. Instability of shock train behaviour with incident shocks. *Journal of Fluid Mechanics*, 907:A40, 2021.

[36] Nan Li and Juntao Chang. Hysteretic behaviors of separation-shock driven by backpressure in isolator with incident shocks. *AIAA Journal*, 59(3):960–971, 2020.

[37] Robin L Hunt and Mirko Gamba. On the origin and propagation of perturbations that cause shock train inherent unsteadiness. *Journal of Fluid Mechanics*, 861:815–859, 2019.

[38] A Weiss and H Olivier. Behaviour of a shock train under the influence of boundary-layer suction by a normal slot. *Experiments in fluids*, 52(2):273–287, 2012.

[39] Vignesh Ram Petha Sethuraman, Yosheph Yang, and Jae Gang Kim. Low-frequency shock train oscillation control in a constant area duct. *Physics of Fluids*, 34(1):016105, 2022.

[40] Yubao He, Hongyan Huang, and Daren Yu. Investigation of corner separation and suction control in constant area duct. *Aerospace Science and Technology*, 66:70–82, 2017.

[41] hao Xu, Zhaobo Du, Xiangyu Zhong, and Wei Huang. Research progress of microjet control of shock/boundary layer interactions in supersonic flow field (in chinese). *Aero Weaponry*, pages 1–10, 2022.

[42] Yanming Liu, Hong Zhang, and Pingchao Liu. Flow control in supersonic flow field based on micro jets. *Advances in Mechanical Engineering*, 11(1):1687814018821526, 2019.

[43] SB Verma and C Manisankar. Control of compression-ramp-induced interaction with steady microjets. *AIAA Journal*, 57(7):2892–2904, 2019.

[44] Meng-Sing Liou. A sequel to ausm: Ausm+. *Journal of computational Physics*, 129(2):364–382, 1996.

[45] P. J. Roache. Perspective: A method for uniform reporting of grid refinement studies. *Journal of Fluids Engineering*, 116(3):405–413, 1994.